This is the author's version of an article that has been published in this journal. Changes were made to this version by the publisher prior to publication.
The final version of record is available at http://dx.doi.org/10.1109/TVCG.2014.2346415

Vortex Cores of Inertial Particles

Tobias Günther and Holger Theisel

Abstract— The cores of massless, swirling particle motion are an indicator for vortex-like behavior in vector fields and to this end, a number of coreline extractors have been proposed in the literature. Though, many practical applications go beyond the study of the vector field. Instead, engineers seek to understand the behavior of inertial particles moving therein, for instance in sediment transport, helicopter brownout and pulverized coal combustion. In this paper, we present two strategies for the extraction of the corelines that inertial particles swirl around, which depend on particle density, particle diameter, fluid viscosity and gravity. The first is to deduce the local swirling behavior from the autonomous inertial motion ODE, which eventually reduces to a parallel vectors operation. For the second strategy, we use a particle density estimation to locate inertial attractors. With this, we are able to extract the cores of swirling inertial particle motion for both steady and unsteady 3D vector fields. We demonstrate our techniques in a number of benchmark data sets, and elaborate on the relation to traditional massless corelines.

Index Terms—Inertial particles, flow visualization, vortex cores

1 Introduction

The motion of solid inertial particles in gas or fluid flows is an important field of research, since they are involved in numerous scientific and industrial applications, such as combustion of pulverized coal, sediment transport, helicopter brownout, sand blasting, particulate pollution control, soiling of cars and many more [24, 27, 20]. In contrast to massless particles, the objective is not to visualize the flow, but to draw conclusions on the behavior of the inertial particles moving therein. However, massless particles have been studied by the flow visualization community for decades, which created a pool of concepts that we can draw on to develop new visualizations that facilitate the assessment of inertial particle dynamics. Among these concepts is the extraction of vortex core lines. Although different definitions exist, one popular understanding is that these are the lines where particles swirl around. In the past, several methods have been proposed to extract them, including two classes of approaches: the local and integration-based methods. Both of the approaches extract their own subset of vortices. The local methods detect steady vortices or vortices moving along straight lines. The integration-based methods find only attracting corelines, though for every kind of vortex motion. Since it was shown that the swirling behavior is mass-dependent [9], we can expect that the location of vortex cores also depends on the mass of the considered particles.

For the purpose of understanding the swirling behavior of inertial particles, we extend both the local Sujudi-Haimes [26] and the integration-based particle density estimation [33] to the inertial case. While for massless particles, the particle position only depends on the vector field, inertial particles have their own velocity vector, which is affected over time by inertia. The integration therefore requires to model position, current velocity and optionally time as state variables, rendering the system 6D or 7D. Detecting the swirling behavior within this high-dimensional space is accompanied by a large computation effort—at least for the brute force search that follows from a direct extension of the Sujudi-Haimes method from the massless case. However, we show that the search can actually be reduced to a 3D (or 4D) parallel vectors operation, if additional knowledge is carefully included. In consequence, we found a method that is computationally as expensive as an extraction of massless corelines, but can answer the same question for inertial particles. Moreover, due to the rich set of long known extraction methods via parallel vectors [18], it is easily integrated into existing visualization tools.

As a second strategy for finding core lines, we apply an integration-based particle density estimation after a short integration span to inertial particles, in order to find attracting structures that the local methods cannot correctly extract (not even for the massless case). In the remainder of the paper, we introduce the extraction methods and conduct a qualitative evaluation on a number of benchmark data sets.

Notation: We denote a point/vector in 3D space by bold letters, e.g., $\mathbf{x}, \mathbf{u}$. Points/vectors in 4D space-time are written as $\bar{\mathbf{x}}, \bar{\mathbf{u}}$, i.e., the last component refers to time. Since for inertial particles the direction of movement does not only depend on the vector field $\mathbf{u}$ but also depends on the current particle velocity $\mathbf{v}$, we denote 6D points/vectors as $\tilde{\mathbf{x}}, \tilde{\mathbf{u}}$ where the first 3 components refer to the spatial locations and the last 3 refer to the current particle velocity. Similar considerations for time-dependent flow fields give 7D points/vectors $\hat{\mathbf{x}}, \hat{\mathbf{u}}$ where the additional last component refers to time.

We use the concept of the parallel vectors (PV) operator. Thereby, $\mathbf{v}_1 \parallel \mathbf{v}_2$ denotes that the vectors $\mathbf{v}_1, \mathbf{v}_2$ are linearly dependent. Note that the PV operator works in any dimensionality, and that basic computation rules apply: $\mathbf{v}_1 \parallel \mathbf{v}_2 \Longleftrightarrow \mathbf{v}_1 \parallel (\alpha\mathbf{v}_1 + \beta\mathbf{v}_2)$ for any real α, β and $\mathbf{v}_1 \neq \mathbf{0}$.

2 Related Work

Vortices are flow phenomena that are studied in many engineering problems, for instance, they entrain dust in helicopter landing maneuvers, create noise at rotor blade-vortex interaction, and are reduced by winglet design on airplanes to increase the efficiency of the machines. A number of formal vortex definitions exist in the literature [10, 12, 13, 21], and several extraction methods have been proposed that can be categorized into region-based methods or line-based methods.

Region-based methods extract a volume of vortex-like behavior. Simple examples are thresholding pressure, vorticity or helicity, though they require a threshold to be set that is not necessarily constant along the vortex, thus they are rather impractical. In the CFD community, other region-based measures are more established, e.g., the Q-criterion [12] and λ_2-criterion [13].

Line-based methods search for the center line of swirling motion within a vortex. For this, Banks and Singer [1] suggested a curve following velocity-predictor, pressure-corrector method. Sahner et al. [22] extracted extremum lines of the λ_2-criterion and Q-criterion by the use of feature flow fields [29]. Sahner et al. [23] extracted both vortex and strain features as extremal structures of derived scalar quantities in order to create vortex and strain skeletons.

Sujudi and Haimes [26] introduced the reduced vorticity criterion that considers the eigenvalues of the Jacobian $\mathbf{J}$ of the flow $\mathbf{u}$. Here,

- *Tobias Günther is with the Visual Computing Group at the University of Magdeburg. E-mail: tobias@isg.cs.ovgu.de.*
- *Holger Theisel is head of the Visual Computing Group at the University of Magdeburg. E-mail: theisel@isg.cs.ovgu.de.*

Manuscript received 31 Mar. 2014; accepted 1 Aug. 2014; date of publication xx xxx 2014; date of current version xx xxx 2014.
For information on obtaining reprints of this article, please send e-mail to: tvcg@computer.org.

Copyright (c) 2014 IEEE. Personal use is permitted. For any other purposes, permission must be obtained from the IEEE by emailing pubs-permissions@ieee.org.

This is the author's version of an article that has been published in this journal. Changes were made to this version by the publisher prior to publication.
The final version of record is available at http://dx.doi.org/10.1109/TVCG.2014.2346415

a vortex coreline is present if a pair of complex-conjugate eigenvalues exists and the eigenvector $\mathbf{e}$ to the remaining real eigenvalue fulfills: $\mathbf{u}-(\mathbf{u}^{\mathrm{T}}\mathbf{e})\mathbf{e}=\mathbf{0}$. This method finds the center of swirling streamlines. Peikert and Roth [18] formally introduced the parallel vectors (PV) operator, which returns the set of points at which two vector fields are parallel. They summarized different algorithms for the extraction of these locations, including an analytic solution for triangles. The PV operator allows to express Sujudi-Haimes equivalently as $\mathbf{u} \parallel \mathbf{J}\mathbf{u}$.

For unsteady data, Bauer and Peikert [2], and Theisel et al. [28] tracked the cores of swirling streamlines over time. However, Fuchs et al. [8] and Weinkauf et al. [30] realized that pathlines swirl around a different coreline and thus extended the concept of Sujudi and Haimes in different ways to find cores of swirling pathlines. Here, we follow [30] who eventually derived a coplanarity condition that reduces to a parallel vectors operator.

In experimental flow visualization, vortices are made visible by injection of ink or smoke into the air or fluid. Following the same idea, it is possible to inject particles in computational flow visualization and to observe their behavior. If the vortex is attracting, the center line can be found by integration-based methods, e.g., by measuring the density of particles after a short integration, as in Wiebel et al. [33]. Weinkauf and Theisel [31] found these attractors by analyzing the Jacobian of a derived vector field in which streaklines are tangent curves. For a more detailed overview on vortex extraction methods we refer to [15, 18, 19].

So far, all approaches were developed for massless particles. However, Günther et al. [9] demonstrated that the cores of inertial particles are mass-dependent and therefore not detectable by the existing methods. In this paper, we extend the local Sujudi-Haimes method to the mass-dependent case and apply an integration-based density estimation to find attracting corelines.

3 Inertial Particles

The motion of spherical, inertial particles in fluid flows is governed by the Maxey-Riley equations [16]. They involve a number of forces, such as the force exerted by the flow itself, buoyancy, Stokes drag, the force exerted due to the mass of the fluid moving with the particle and the Basset-Boussinesq memory term (cf. Haller and Sapsis [11]). Depending on the application, several assumptions can be made. We assume particles to be spherical and very small in size, which allows to assume Stokes flow due to their small particle Reynolds number. Also, the particle density is assumed to be far higher than the fluid density, which allows to neglect buoyancy. Further assuming dilute flow, the particle motion is dominated by drag forces, rather than particle-particle collision. Thus, we can neglect collision handling and assume one-way coupling, i.e., the particles do not affect the surrounding fluid. These simplifications are common and were used for instance in [27, 14, 6, 4, 3]. They lead to the following equations of motion according to Crowe et al. [7]:

$$\frac{\mathrm{d}\mathbf{x}}{\mathrm{d}t} = \mathbf{v}(t) \qquad \text{with} \quad \mathbf{x}(0)=\mathbf{x}_0 \tag{1}$$

$$\frac{\mathrm{d}\mathbf{v}}{\mathrm{d}t} = \frac{\mathbf{u}(\mathbf{x}(t),t)-\mathbf{v}(t)}{r}+\mathbf{g} \qquad \text{with} \quad \mathbf{v}(0)=\mathbf{v}_0 \tag{2}$$

where $\mathbf{u}$ is the time-dependent flow field, $\mathbf{v}$ is the current particle velocity, $\mathbf{g}$ is the gravity vector and r is the particle response time. The response time is characterized by the diameter d_p and density ρ_p of the particle, as well as the viscosity ν of the fluid:

$$r=\frac{d_p^2\rho_p}{18\nu}. \tag{3}$$

The response time is the time required for a particle released from rest in a gravity-free environment to acquire 63% of the velocity of the carrying fluid, cf. [7]. For all examples in the paper, we used as particle density ρ_p the density of quartz glass, i.e., $\rho_p = 2650\,kg/m^3$. The diameter d_p varies between $d_p = 0\,\mu m$ and $d_p = 300\,\mu m$. Note that the equations of motion hold for $d_p \ll \eta_k$, with η_k being the Kolmogorov length scale. The surrounding medium was assumed to be air, thus the viscosity was set to $\nu = 1.532\cdot 10^{-5}\,kg/(m\cdot s)$.

The equations of motion (1) and (2) can be written in an autonomous system making all location, current particle velocity and time a state variable:

$$\frac{\mathrm{d}}{\mathrm{d}t}\begin{pmatrix}\mathbf{x}\\ \mathbf{v}\\ t\end{pmatrix} = \begin{pmatrix}\mathbf{v}\\ \frac{\mathbf{u}(\mathbf{x},t)-\mathbf{v}}{r}+\mathbf{g}\\ 1\end{pmatrix} \qquad \text{with} \quad \begin{pmatrix}\mathbf{x}\\ \mathbf{v}\\ t\end{pmatrix}(0) = \begin{pmatrix}\mathbf{x}_0\\ \mathbf{v}_0\\ t_0\end{pmatrix}. \tag{4}$$

Then, mass-dependent pathlines arise as tangent curves of this 7-dimensional vector field.

An alternative approach is to add the material derivative $\mathrm{D}\mathbf{u}/\mathrm{D}t$ of the fluid to the particle equations in order to indirectly model gravity (and/or buoyancy) as external force. Thereby, fluid motion (in Eulerian frame) and particle motion (in Lagrangian frame) are made consistent, cf. Benzi et al. [4]. As we later synthetically alter the gravity to generate new test cases (without recomputing the fluid flow), we use equations of particle motion that model gravity explicitly [7]. This method is simpler in its modelling, but holds for the given assumptions.

3.1 Relation to Massless Particles

Inertial particles are not used to explore the properties of a vector field, but to assess the motion of inertial objects therein. Massless particles, on the other hand, are used for the visualization of the underlying vector field, as their trajectory is tangential to the flow. When approaching zero response time $r \to 0$, the inertial equations of motion approach the massless case. This is shown by rearranging Eq. (2) for $\mathbf{v}$ and substituting in Eq. 1, which yields in the limit tangent curves of $\mathbf{u}$:

$$\lim_{r\to 0}\frac{\mathrm{d}\mathbf{x}}{\mathrm{d}t} = \mathbf{u}(\mathbf{x}(t),t)\underbrace{-r\frac{\mathrm{d}\mathbf{v}}{\mathrm{d}t}+r\,\mathbf{g}}_{0}. \tag{5}$$

However, the smaller the response time becomes, the more numerical problems occur, since Eq. (4) contains a division by the response time. Such a singular perturbation problem is avoided by scaling the time step (cf. Haller and Sapsis [11]). Assuming, a very small response time $r = \varepsilon \ll 1$. The usual approach to integrate Eq.(4) is to use:

$$\frac{\mathrm{d}}{\mathrm{d}t}\begin{pmatrix}\mathbf{x}\\ \mathbf{v}\\ t\end{pmatrix} = \begin{pmatrix}\varepsilon\,\mathbf{v}\\ \mathbf{u}(\mathbf{x},t)-\mathbf{v}+\varepsilon\,\mathbf{g}\\ \varepsilon\end{pmatrix}. \tag{6}$$

Thereby, the integration of an inertial path can be very expensive due to the potentially small step size. In the practical use, the difference to massless trajectories becomes neglectable for very small particles. Thus, at some point (depending on particle diameter, particle density and viscosity), massless trajectories can be used instead.

4 Cores of Inertial Swirling Particles

Even for massless particles there is no universal coreline extraction or vortex criterion. Several approaches exist, all having their benefits and problems. The *local methods* only work for static corelines or corelines that move along straight lines. *Integration-based methods*, on the other hand, only detect attracting behavior. Though, at present, these are the best-established approaches. However, none is directly applicable to inertial particles, which is why we extend both approaches to the inertial case. In this section, we will show that the extraction of vortex corelines of inertial particles reduces to a parallel vectors operation in space (3D) for steady or space-time (4D) for unsteady flows.

4.1 Local Methods in a Nutshell

Given a (steady or unsteady) flow field $\mathbf{u}$ with its spatial Jacobian matrix $\mathbf{J}$, the (necessary) local conditions for corelines are summarized in Table 1. Here, r is the response time (3), $\mathbf{g}$ the gravity vector, and $\mathbf{f}$ is defined as suitable combination of the partial derivatives of $\mathbf{u}$:

$$\mathbf{f} = \frac{1}{\det\mathbf{J}}\begin{pmatrix}-\det(\mathbf{u}_y,\mathbf{u}_z,\mathbf{u}_t)\\ +\det(\mathbf{u}_z,\mathbf{u}_t,\mathbf{u}_x)\\ -\det(\mathbf{u}_t,\mathbf{u}_x,\mathbf{u}_y)\end{pmatrix}. \tag{7}$$

Copyright (c) 2014 IEEE. Personal use is permitted. For any other purposes, permission must be obtained from the IEEE by emailing pubs-permissions@ieee.org.

This is the author's version of an article that has been published in this journal. Changes were made to this version by the publisher prior to publication.
The final version of record is available at http://dx.doi.org/10.1109/TVCG.2014.2346415

	massless	inertial
steady	$\mathbf{u} \parallel \mathbf{J}\mathbf{u}$	$(\mathbf{u}+r\,\mathbf{g}) \parallel \mathbf{J}(\mathbf{u}+r\,\mathbf{g})$
unsteady	$(\mathbf{u}-\mathbf{f}) \parallel \mathbf{J}(\mathbf{u}-\mathbf{f})$	$(\mathbf{u}-\mathbf{f}+r\,\mathbf{g}) \parallel \mathbf{J}(\mathbf{u}-\mathbf{f}+r\,\mathbf{g})$

Table 1. Conditions for the presence of a core of swirling particle motion for massless [26, 30] and inertial particles: $\mathbf{u}$ denotes the vector field, $\mathbf{J}$ its spatial Jacobian, $\mathbf{f}$ the feature flow field, r the response time, $\mathbf{g}$ the gravity vector. Note that in addition, the extracted line has to approximately align with the parallel vectors and that $\mathbf{J}$ must contain complex-conjugate eigenvalues.

Note that Table 1 only gives necessary conditions: the extracted line structures have to be filtered by the presence of swirling motion, i.e., the existence of imaginary eigenvalues of $\mathbf{J}$ and the tangent of the extracted coreline should approximately align with the parallel vectors. In Table 1, the condition for the steady massless case is the Sujudi-Haimes condition [26]. Its extension from [30] is the condition for the unsteady massless case. The two conditions for the inertial case (right-hand column of Table 1) are the main theoretical contributions of this paper. Fortunately, they do not depend on the current particle velocity $\mathbf{v}$, leading to a simple 3D PV extraction which can be done by standard methods. Although the conditions for inertial particles are extremely simple, their derivations are not. They are presented in the subsequent sections 4.2 and 4.3. To extract attracting corelines we apply an integration-based method that works in both steady and unsteady flows, as described in Section 4.4.

4.2 Local Method for Steady Case

For steady flows, we generalize the well-established Sujudi-Haimes approach [26] to inertial particles. Following (4), we consider the 6D steady vector field, in which inertial particle trajectories are tangent curves:

$$\tilde{\mathbf{u}}(\mathbf{x},\mathbf{v}) = \begin{pmatrix} \mathbf{v} \\ \frac{\mathbf{u}(\mathbf{x})-\mathbf{v}}{r} + \mathbf{g} \end{pmatrix}. \tag{8}$$

Its Jacobian is the 6×6 matrix

$$\tilde{\mathbf{J}} = \begin{pmatrix} \mathbf{0}_{3,3} & \mathbf{I}_3 \\ \frac{1}{r}\mathbf{J} & -\frac{1}{r}\mathbf{I}_3 \end{pmatrix}. \tag{9}$$

where $\mathbf{0}_{3,3}$ is the zero matrix, $\mathbf{I}_3$ the identity matrix, and $\mathbf{J}$ the 3×3 Jacobian of $\mathbf{u}$. (The derivation is included in the additional material.)

The Jacobian $\tilde{\mathbf{J}}$ characterizes the inertial particle behavior in both the spatial and the velocity domain. Extending the Sujudi-Haimes approach to 6D, we search for all 6D locations where $\tilde{\mathbf{u}}$ is parallel to a real eigenvector of $\tilde{\mathbf{J}}$, i.e., we search for 6D locations with

$$\tilde{\mathbf{u}} \parallel \tilde{\mathbf{J}}\tilde{\mathbf{u}}. \tag{10}$$

Using the abbreviation

$$\mathbf{w} = \frac{\mathbf{u}-\mathbf{v}}{r} + \mathbf{g} \tag{11}$$

we get

$$\tilde{\mathbf{u}} = \begin{pmatrix} \mathbf{v} \\ \mathbf{w} \end{pmatrix}, \quad \tilde{\mathbf{J}}\,\tilde{\mathbf{u}} = \begin{pmatrix} \mathbf{w} \\ \frac{1}{r}(\mathbf{J}\mathbf{v}-\mathbf{w}) \end{pmatrix}. \tag{12}$$

(The derivation of this is also in the additional material.) From the parallelity (10) follows the parallelity in all projections to subspaces. Projecting (10) into the spatial subspace gives

$$\mathbf{v} \parallel \mathbf{w} \tag{13}$$

which simplifies under the consideration of (11) to

$$\mathbf{v} \parallel \mathbf{u}(\mathbf{x}) + r\,\mathbf{g}\,. \tag{14}$$

At the moment, this condition requires a particle velocity $\mathbf{v}$ at position $\mathbf{x}$, which is problematic. We cannot evaluate the condition without a brute-force simulation of a large number of particles in order to observe the different velocities of particles passing location $\mathbf{x}$. We circumvent the problem of not knowing $\mathbf{v}$ by introducing another condition: we project the condition (10) into the $\mathbf{v}$ subspace. Considering (12), this gives the condition

$$\mathbf{w} \parallel \frac{1}{r}(\mathbf{J}\mathbf{v}-\mathbf{w}). \tag{15}$$

By inserting (13) into (15) we get

$$\mathbf{v} \parallel \frac{1}{r}(\mathbf{J}\mathbf{v}-\mathbf{v}) \tag{16}$$

which further simplifies to

$$\mathbf{v} \parallel \mathbf{J}\mathbf{v}. \tag{17}$$

Finally, we combine the parallelity conditions of both subspaces by inserting (14) into (17), which gives the final condition

$$(\mathbf{u}+r\,\mathbf{g}) \parallel \mathbf{J}(\mathbf{u}+r\,\mathbf{g}). \tag{18}$$

Note that (18) does not contain $\mathbf{v}$ any more: it can be solved in the spatial domain only by applying standard 3D PV techniques.

For massless particles, the response time is $r = 0$. In this case, (18) becomes $\mathbf{u} \parallel \mathbf{J}\mathbf{u}$, which is the parallel vectors expression of Sujudi-Haimes. Thus, the swirling of massless particles is a special case of our generalized parallel vectors condition.

Condition (18) also reduces to $\mathbf{u} \parallel \mathbf{J}\mathbf{u}$ if there is no gravity, i.e., $\mathbf{g} = \mathbf{0}$. This means that all inertial particles, regardless of their response time (i.e., diameter or density), swirl in gravity-free environments around the same coreline. We demonstrate this effect in Fig. 1. The trajectories of inertial particles change with a varying particle diameter, but the coreline remains the same.

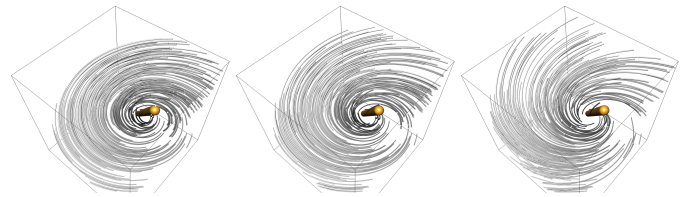

Fig. 1. For $\mathbf{g} = \mathbf{0}$ inertial particles of any size have the same coreline. Left to right: $d_p = 0\,\mu m$ (massless), $d_p = 100\,\mu m$ and $d_p = 200\,\mu m$.

4.3 Local Method for Unsteady Case

For unsteady flows, we extend the cores of swirling particle motion of [30] to inertial particle flows. For this, we consider the 7D vector field

$$\hat{\mathbf{p}}(\mathbf{x},\mathbf{v},t) = \begin{pmatrix} \mathbf{v} \\ \frac{\mathbf{u}(\mathbf{x},t)-\mathbf{v}}{r} + \mathbf{g} \\ 1 \end{pmatrix}. \tag{19}$$

which is obtained by including time as an explicit state variable. Its Jacobian is the 7×7 matrix (see additional material for a derivation)

$$\hat{\mathbf{J}} = \begin{pmatrix} \mathbf{0}_{3,3} & \mathbf{I}_3 & \mathbf{0}_3 \\ \frac{1}{r}\mathbf{J} & -\frac{1}{r}\mathbf{I}_3 & \frac{1}{r}\mathbf{u}_t \\ \mathbf{0}_3^T & \mathbf{0}_3^T & 0 \end{pmatrix} \tag{20}$$

where $\mathbf{0}_3$ is the 3D zero (column) vector and $\mathbf{u}_t = \frac{\partial \mathbf{u}}{\partial t}$ is the t-partial of $\mathbf{u}$. Following [30], we use the *coplanar vector operator* for detecting vortex structures: we search for 7D locations where we can find two real eigenvectors $\hat{\mathbf{e}}_i, \hat{\mathbf{e}}_j$ of $\hat{\mathbf{J}}$ such that $\hat{\mathbf{e}}_i, \hat{\mathbf{e}}_j, \hat{\mathbf{p}}$ are coplanar, i.e.,

$$\hat{\mathbf{p}} = \beta\,\hat{\mathbf{e}}_i + \gamma\,\hat{\mathbf{e}}_j \tag{21}$$

for certain scalars β, γ. The eigenvectors of $\hat{\mathbf{J}}$ are

$$\begin{pmatrix} \tilde{\mathbf{e}}_1 \\ 0 \end{pmatrix}, \ldots, \begin{pmatrix} \tilde{\mathbf{e}}_6 \\ 0 \end{pmatrix}, \hat{\mathbf{e}}_7 = \begin{pmatrix} \mathbf{f} \\ \mathbf{0}_3 \\ 1 \end{pmatrix} \tag{22}$$

Copyright (c) 2014 IEEE. Personal use is permitted. For any other purposes, permission must be obtained from the IEEE by emailing pubs-permissions@ieee.org.

This is the author's version of an article that has been published in this journal. Changes were made to this version by the publisher prior to publication.
The final version of record is available at http://dx.doi.org/10.1109/TVCG.2014.2346415

where $\tilde{\mathbf{e}}_1, \ldots, \tilde{\mathbf{e}}_6$ are the eigenvectors of $\tilde{\mathbf{J}}$, and $\hat{\mathbf{e}}_7$ is the eigenvector belonging to the eigenvalue 0, i.e., the solution of $\hat{\mathbf{J}}\,\hat{\mathbf{e}}_7 = \mathbf{0}_7$. The explicit solution of this equation gives the vector $\mathbf{f}$ as defined in (7). Note that it has been used elsewhere [32] to track critical points in 3D unsteady vector fields. Considering the last components of (22) and (21) gives $j = 7$ and $\gamma = 1$ in (21). Applying this to the first 6 components of (21) gives the condition

$$\tilde{\mathbf{u}} - \begin{pmatrix} \mathbf{f} \\ \mathbf{0}_3 \end{pmatrix} \parallel \tilde{\mathbf{e}}_i \tag{23}$$

where $\tilde{\mathbf{e}}_i$ is a real eigenvector of $\tilde{\mathbf{J}}$. (23) means that we have reduced the 7D coplanar vectors problem to a 6D PV problem. Similar to Section 4.2, this is now further reduced to a 3D PV condition which can be searched in 3D space only. (23) can be rewritten as

$$\tilde{\mathbf{u}} - \begin{pmatrix} \mathbf{f} \\ \mathbf{0}_3 \end{pmatrix} \parallel \tilde{\mathbf{J}} \left(\tilde{\mathbf{u}} - \begin{pmatrix} \mathbf{f} \\ \mathbf{0}_3 \end{pmatrix} \right). \tag{24}$$

Since

$$\tilde{\mathbf{J}} \left(\tilde{\mathbf{u}} - \begin{pmatrix} \mathbf{f} \\ \mathbf{0}_3 \end{pmatrix} \right) = \begin{pmatrix} \mathbf{w} \\ \frac{1}{r} \left(\mathbf{J}(\mathbf{v} - \mathbf{f}) - \mathbf{w} \right) \end{pmatrix} \tag{25}$$

(as shown in the additional material), with $\mathbf{w}$ defined in (11), condition (24) can be projected into their $\mathbf{x}$ and $\mathbf{v}$ subspace respectively:

$$\mathbf{v} - \mathbf{f} \quad \parallel \quad \mathbf{w} \tag{26}$$

$$\mathbf{w} \quad \parallel \quad \frac{1}{r} (\mathbf{J}(\mathbf{v} - \mathbf{f}) - \mathbf{w}). \tag{27}$$

From multiplying (11) by r and substituting in (26) we get

$$(\mathbf{v} - \mathbf{f}) \parallel (\mathbf{u} - \mathbf{v} + r\,\mathbf{g}) \tag{28}$$

To obtain a condition in which one side is independent of $\mathbf{v}$, we add the left-hand side $(\mathbf{v} - \mathbf{f})$ to the right-hand side of (28)

$$(\mathbf{v} - \mathbf{f}) \parallel (\mathbf{u} - \mathbf{f} + r\,\mathbf{g}). \tag{29}$$

Inserting (26) into (27) and multiplying the right-hand side by r gives

$$(\mathbf{v} - \mathbf{f}) \parallel (\mathbf{J}(\mathbf{v} - \mathbf{f}) - \mathbf{w}). \tag{30}$$

Considering (26) again, we see that the $\mathbf{w}$ on the right of (30) is parallel to the left-hand side and can thus be removed

$$(\mathbf{v} - \mathbf{f}) \parallel \mathbf{J}(\mathbf{v} - \mathbf{f}). \tag{31}$$

Inserting (29) into (31) gives the final condition

$$(\mathbf{u} - \mathbf{f} + r\,\mathbf{g}) \parallel \mathbf{J}(\mathbf{u} - \mathbf{f} + r\,\mathbf{g}). \tag{32}$$

Note that (32) does not contain $\mathbf{v}$ any more: it can be solved by applying a standard PV extractor in 3D space and subsequently filtering the resulting lines by swirling motion, i.e., the presence of imaginary eigenvalues of $\mathbf{J}$.

For massless particles, i.e., $r = 0$, or in a gravity-free environment, i.e., $\mathbf{g} = \mathbf{0}$, the generalized Eq. (32) reduces to the parallel vectors condition of cores of swirling, massless pathlines: $(\mathbf{u} - \mathbf{f}) \parallel \mathbf{J}(\mathbf{u} - \mathbf{f})$, which was described in [30]. This is similar to the steady case, shown in Section 4.2.

4.4 Integration-based Method

Attracting corelines can be found for both steady and unsteady flows in a number of different, yet quite similar ways: all have in common that they are integration-based. One option is to apply the particle density estimation of Wiebel et al. [33] to inertial particles, which works as follows: To extract the attractors at time t, seed a large number of particles at time $t - \tau$ on a regular grid that spans the entire spatial domain. Note that inertial corelines are found at the accuracy of the resolution of the seeding grid. Integrate all particles for a duration τ up to the time t. During this time, the particles will converge to the attracting structures, thus their density will increase near them and will eventually obtain its maximum directly on them. The density can be obtained by rasterization of the particles into a second grid, which is used for counting rasterized particles. Local maxima are found by inspecting each density grid cell in turn in order to search for cells that have a higher density than all adjacent cells. Optionally, the density field can be smoothed prior to the maxima extraction if too many local extrema exist. For the tracking of attractors over time, the procedure is repeated for a series of observation times. For each time step, attractors are extracted and are connected over time by lines by using a correspondence heuristic, e.g., by joining with the closest attractor of the previous observation time.

Another variant of the density estimation is to seed at each cell of a regular grid a small group of particles and to await their contraction: if the particles within a group get very close to each other, e.g., the maximum pairwise distance falls below a threshold, an attractor is found at subgrid accuracy. Moreover, the full coreline can be found by continuing the integration until the particles leave the (temporal) domain, since they will stay on the attractor. Afterwards, identical lines have to be removed. In this approach, the integration duration and the extend of the group's seed structure should be chosen carefully. The closer particles are seeded, the shorter the duration until they contract. If they are seeded too far apart, the temporal domain might not be long enough for the particles to collapse. For time-periodic fields, this is not a problem, since the integration can be continued until an attractor is found. This is the approach that we followed in the paper.

A third option that was successfully applied to the massless case is to consider the cores of swirling streaklines [31]. For this a derived vector field is constructed, in which streaklines are tangent curves. Then, the swirling in this derived vector field is observed, which—for the massless case—reduced to a parallel vectors operation. This strategy has a high computational effort, but an extension to the inertial case is worth a study in future work.

5 Results and Discussion

In the following, we show extraction results for a number of test data sets, as we alter the gravity that acts on the inertial particles. Note that the gravity we choose in the test cases is not the same as was used in the computation of the given vector field. They need to be consistent in order to draw meaningful conclusions for the application. By varying the gravity only in the particle motion, we obtain a different flow setting that, given the gravity, coincides after running a new fluid simulation with the flow field that was originally given. Thus, it is not possible to infer statements on the original field. However, it allows us to generate more synthetic test data, in which we seed inertial particles and extract their cores. The goal of our qualitative evaluation is not to come up with new insights for the applications, but to show that given a flow and a gravity: we can compute the cores of inertial particles.

5.1 Moving Center (2D unsteady)

Weinkauf et al. [30] used an analytic unsteady 2D field to demonstrate their extraction of the centers of swirling (massless) pathlines. They illustrated its construction, which is a linear interpolation over time between two 2D centers. The flow is defined on the domain $D \times T = [-2,2]^2 \times [0,4]$, with centers located at $(1,-1,0)^{\mathrm{T}}$ and $(-1,1,4)^{\mathrm{T}}$:

$$\mathbf{u}(x,y,t) = \begin{pmatrix} -y + \frac{t}{2} - 1 \\ x + \frac{t}{2} - 1 \end{pmatrix}. \tag{33}$$

In this data set, the massless coreline is a line that travels on a straight line, thus Sujudi-Haimes is known to work perfectly [30]. By using it, we find for this simple vector field the family of corelines analytically as $\mathbf{c}(a,s) = ((a-s+2)/2, (a+s-2)/2, s)^{\mathrm{T}}$, with $a = 1 + r\,\mathbf{g}_z$. When varying gravity or mass, corelines might move in an unanticipated direction. Here, both gravity $\mathbf{g} = (0,0,\mathbf{g}_z)^{\mathrm{T}}$ and coreline tangent $\partial\mathbf{c}/\partial s = (-1/2, 1/2, 1)^{\mathrm{T}}$ are even perpendicular to the movement direction $\partial\mathbf{c}/\partial a = (1/2, 1/2, 0)^{\mathrm{T}}$ that arises when varying particle diameter or gravity. Such perpendicularity is not generally the case.

Copyright (c) 2014 IEEE. Personal use is permitted. For any other purposes, permission must be obtained from the IEEE by emailing pubs-permissions@ieee.org.

This is the author's version of an article that has been published in this journal. Changes were made to this version by the publisher prior to publication.
The final version of record is available at http://dx.doi.org/10.1109/TVCG.2014.2346415

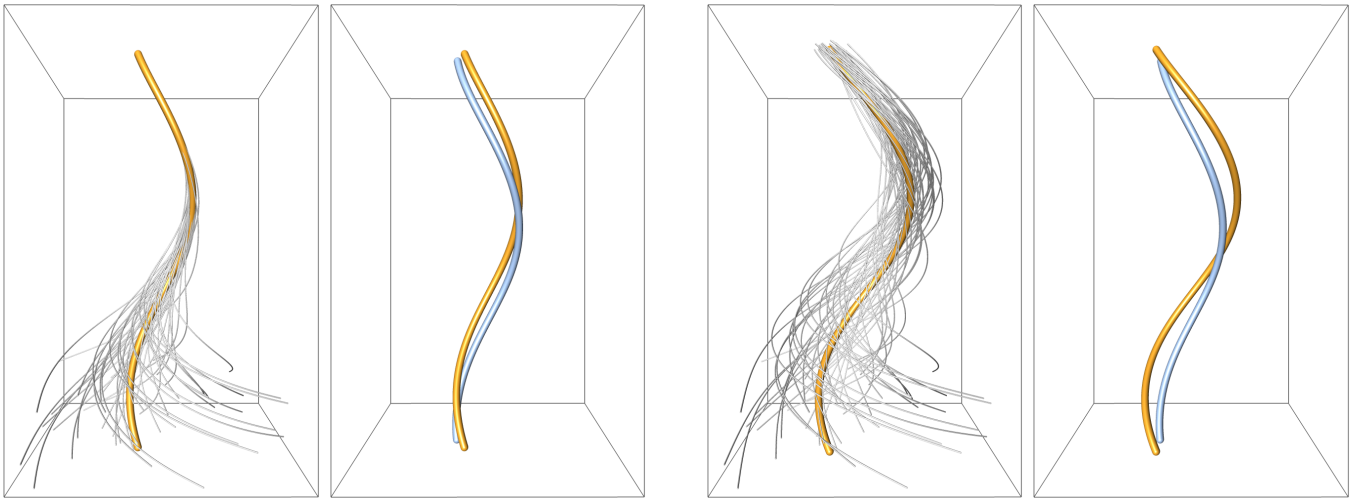

(a) Inertial particle trajectories with $d_p = 100\,\mu m$.

(b) Inertial particle trajectories with $d_p = 200\,\mu m$.

Fig. 3. In the BEADS FLOW, the integration-based particle density estimation (●) successfully detects the attractor of the ascending and thereby converging inertial particles, whereas the local method (●) fails. Since $\mathbf{g} = \mathbf{0}$, the locally extracted coreline (●) is the same for every mass. It can be seen that the integration-based coreline (●) is mass-dependent and that for larger particles, the particles converge slower onto the attracting line.

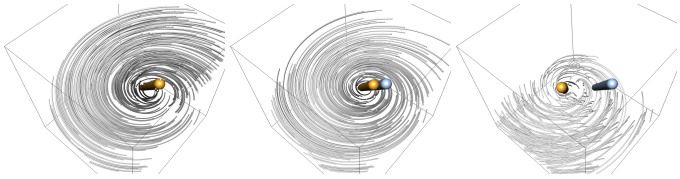

(a) $\mathbf{g} = (0,0,-4)^{\mathrm{T}}$, left to right: $d_p = 0\,\mu m$, $d_p = 100\,\mu m$, $d_p = 200\,\mu m$

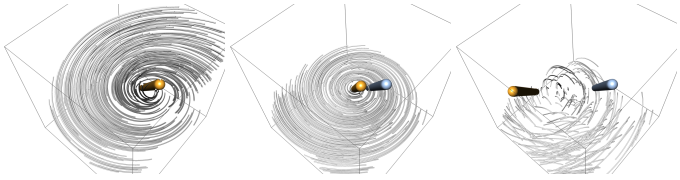

(b) $\mathbf{g} = (0,0,-8)^{\mathrm{T}}$, left to right: $d_p = 0\,\mu m$, $d_p = 100\,\mu m$, $d_p = 200\,\mu m$

Fig. 2. If a gravity force acts on the inertial particles, the position of the vortex coreline (●) changes when varying the mass. The coreline of massless particles (●) is shown as a reference.

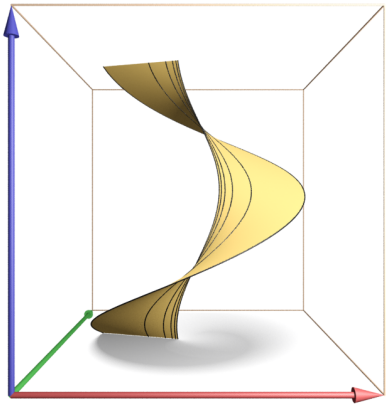

Fig. 4. The attracting corelines that were found in the BEADS FLOW by our integration-based method are mass-dependent and assemble a surface. Here, this surface is shown for $d_p = 100\ldots300\,\mu m$ in the extended domain $D \times T = [-3,3]^2 \times [0,2\pi]$.

In Fig. 1 we have shown that for no gravity, i.e., $\mathbf{g} = \mathbf{0}$, all inertial particles regardless of their size, swirl around a common coreline. If a certain gravity acts, the position of the coreline depends on the mass, as demonstrated in Fig. 2. Similarly, the coreline moves when the mass is constant, but the gravity is varied, as apparent when comparing columns of Figs. 1 and 2.

5.2 Beads Problem (2D unsteady)

A benchmark data set for vortex coreline extraction is the BEADS FLOW. It is a biofluid dynamic model that was reported by Wiebel et al. [33]. In this flow, no standard visualization tool is able to detect the attracting coreline; neither LIC, pathlines, vector field topology nor FTLE. It was shown that neither the tracking of the cores of swirling streamlines over time nor the cores of swirling pathlines match the attractor [31]. Only integration-based methods such as particle density estimation [33] and the cores of swirling streaklines [31] are able to deliver the attracting line. Consequentially, our local inertial methods from Sections 4.2 and 4.3 are not applicable, here. Instead, we will use the integration-based method, introduced in Section 4.4.

An analytic approximation to this data set with similar properties was given in [31]. It is defined in the domain $D \times T = [-2,2]^2 \times [0,2\pi]$:

$$\mathbf{u}(x,y,t) = \begin{pmatrix} -(y - \frac{1}{3}\sin(t)) - (x - \frac{1}{3}\cos(t)) \\ (x - \frac{1}{3}\cos(t)) - (y - \frac{1}{3}\sin(t)) \end{pmatrix}. \tag{34}$$

Günther et al. [9] observed that inertial particles exhibit in the BEADS FLOW a mass-dependent swirling behavior. In Fig. 3(a), we depict swirling inertial particles with $d_p = 100\,\mu m$ and the coreline they attract to. It is shown that the core of swirling inertial pathlines (our local method of Section 4.3) does not match the attractor. Next to it, in Fig. 3(b), we show the same for $d_p = 200\,\mu m$. It can be seen that inertial particles with higher mass, converge slower to their attracting coreline. Moreover, the attracting corelines have a different, mass-dependent radius. In fact, the coreline changes continuously with varying mass, which assembles a surface, shown in Fig. 4. On this surface, isolines are depicted for $d_p = 100, 150, 200, 250, 300\,\mu m$ (from inside to outside). It is apparent that the radius grows exponentially with increasing diameter.

5.3 Helicopter Descent (3D steady)

The HART-II test by Yu et al. [34] was a major experimental cooperation program of rotorcraft engineers from Germany (DLR), the Nether-

Copyright (c) 2014 IEEE. Personal use is permitted. For any other purposes, permission must be obtained from the IEEE by emailing pubs-permissions@ieee.org.

This is the author's version of an article that has been published in this journal. Changes were made to this version by the publisher prior to publication.
The final version of record is available at http://dx.doi.org/10.1109/TVCG.2014.2346415

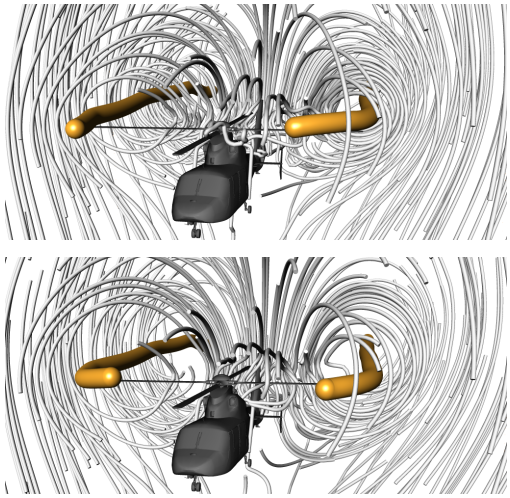

Fig. 5. Vortices detaching from a helicopter in descent. Smaller particles get closer to the corelines, whereas larger particles move on a larger orbit due to inertia. Top $d_p = 0\,\mu m$ (massless), bottom: $d_p = 100\,\mu m$.

lands (ONERA) and the United States (NASA). Its main objective was to study the analytical modeling capabilities of noise and vibrations that arise due to the interaction of rotor blades with wake vortices. The velocity field data was acquired experimentally by particle image velocimetry (PIV) in the German-Dutch Windtunnel (DNW).

We used and modified this data to better suit our visualization purposes. First, the inflow velocity $(0,-0.11,0)^{\mathrm{T}}$ was subtracted in order to make the wake vortices apparent. (The y-axis is the forward flight direction.) Sujudi-Haimes would find the vortices with and without the inflow velocity, though in the original state they are not visible to the eye. Consequentially, the velocity field had to be scaled (by factor 300) in order to get the wind up to speed again, so that the gravity $\mathbf{g} = (-9.8065,0,0)^{\mathrm{T}}$ is not acting overly strong. In Fig. 5, we released particles with $d_p = 0\,\mu m$ (left) and $d_p = 100\,\mu m$ (right). The resulting corelines differ only marginally, though the inertial trajectories exhibit an interesting behavior that we have similarly experienced in the previous BEADS FLOW. Larger particles appear to swirl around the coreline at a larger distance than smaller or massless particles. This seems reasonable due to the acting inertia.

5.4 Delta Wing (3D steady)

The DELTA WING data set is a simulation of a triangular surface in upstream flow. It was provided by Markus Rütten and contains two large wake vortices. The gravity is set to $\mathbf{g} = (0,-9.8065,0)^{\mathrm{T}}$. Originally, this vector field exhibits very high wind speeds. Thus, the trajectories of inertial particles are nearly identical to the massless case. In order to create benchmarking data that showcases inertial corelines that differ from the massless case, we scaled the vector field by 0.006. With this, gravity is proportionally stronger. Pathlines and their corelines are depicted in Fig. 6.

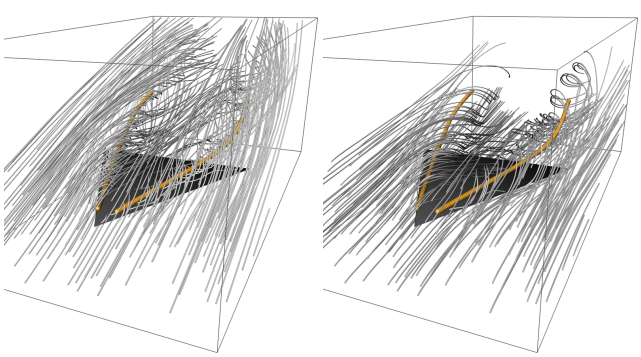

Fig. 6. Two large vortices detach from the DELTA WING surface. Due to gravity inertial particles are forced into a lower altitude. The inertial corelines vary only marginally. Top $d_p = 0\,\mu m$, bottom: $d_p = 100\,\mu m$.

5.5 Hurricane Bonnie (3D steady)

In August 1998, a tropical wave emerged off the coast of Africa and turned into a major hurricane, named Bonnie. Zhu et al. [35, 36] conducted a weather simulation of the northern hemisphere and we picked one particular region of interest that features the hurricane. For this data set, we explored what happens, if gravity is exaggerated. Therefore, we increased the gravity up to $\mathbf{g} = (0,-40,0)^{\mathrm{T}}$, whereas the velocity field was scaled by 0.01, so that small particles of different mass follow trajectories that are apparently different. In Fig. 7, the hurricane is shown from the *same camera view* for two different masses, i.e., for $d_p = 0\,\mu m$ (massless) and $d_p = 20\,\mu m$. The increased gravity in the right image, forces the inertial particles faster to the ground. The extracted corelines are shown, and it is apparent that close to the ground the corelines still match. At higher altitudes, however, they vary considerably.

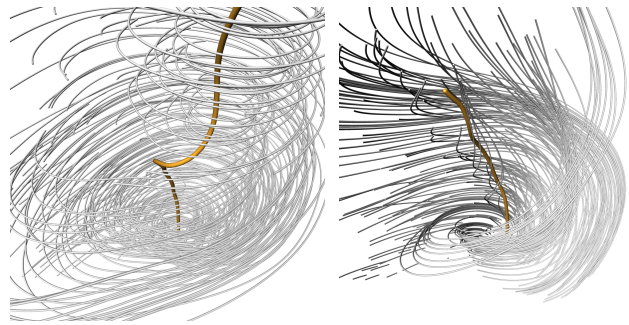

Fig. 7. Corelines for different sizes of a particles. The difference is large to due the high gravity. Left $d_p = 0\,\mu m$ (massless), right: $d_p = 20\,\mu m$.

5.6 Stuart Vortex (3D unsteady)

Another analytic data set that was used in [30] for the extraction of cores of swirling pathlines is the following variant of the STUART VORTEX:

$$\bar{\mathbf{u}}(x,y,z,t) = \begin{pmatrix} \sinh(y)/(\cosh(y) - \frac{1}{4}\cos(x-t)) + 1 \\ -\frac{1}{4}\sin(x-t)/(\cosh(y) - \frac{1}{4}\cos(x-t)) \\ z \\ 1 \end{pmatrix} \tag{35}$$

The vortex is moving constantly over time in x-direction to the right and the vector $(1,0,0)^{\mathrm{T}}$ is superimposed on the spatial coordinates. We consider the domain $D \times T = [-4,4]\times[-2,2]\times[-1,1]\times[0,1]$. For the inertial particles, gravity acts with $\mathbf{g} = (0,9.8065,0)^{\mathrm{T}}$ (the y-axis goes down).

When only considering the streamlines of one time step the swirling cannot be faithfully observed. In Fig. 8 for instance, a center is visible that is not the core of swirling particle motion, seen in Fig. 9(a). However, taking the temporal derivatives into account allows to extract the

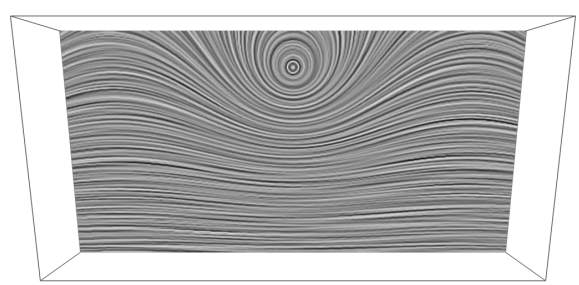

Fig. 8. Line integral convolution of the STUART VORTEX at $t = 0$. Streamlines show a center at the top of the domain.

Copyright (c) 2014 IEEE. Personal use is permitted. For any other purposes, permission must be obtained from the IEEE by emailing pubs-permissions@ieee.org.

This is the author's version of an article that has been published in this journal. Changes were made to this version by the publisher prior to publication.
The final version of record is available at http://dx.doi.org/10.1109/TVCG.2014.2346415

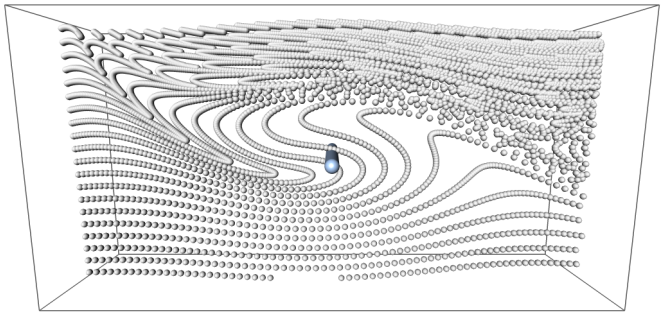

(a) Particles with $d_p = 0\,\mu m$ (massless) swirl around the massless pathline core (•). It can be extracted with [30] and is also a special case of our method.

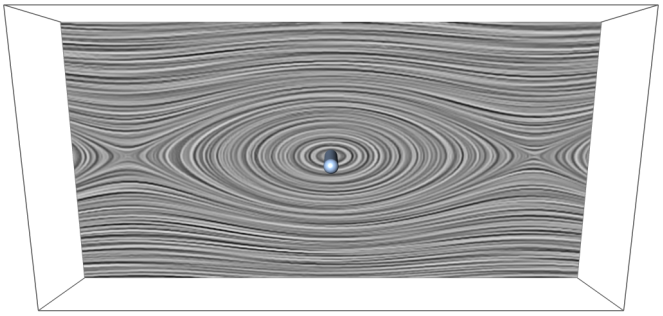

(b) In this image a LIC is utilized to illustrate the vector field $\mathbf{u} - \mathbf{f} + r\,\mathbf{g}$, in which we extract the coreline (•) using the standard PV operator. Note that for $d_p = 0\,\mu m$ the response time is $r = 0$, according to Eq. (3). Thus, for the massless case we find standard pathline cores in $\mathbf{u} - \mathbf{f}$.

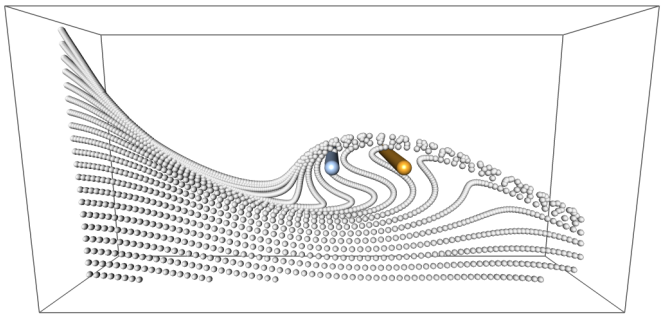

(c) Inertial particles with $d_p = 50\,\mu m$ first fall due to gravity and are then lifted up by the vortex. The common center of rotation is at the inertial coreline (•). The massless pathline core (•) is shown for reference. It is clearly off.

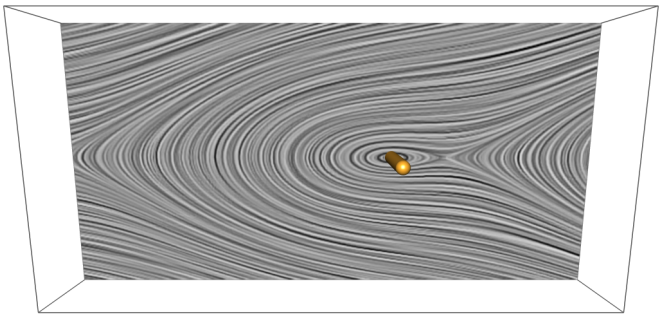

(d) Here, LIC is used to depict the vector field $\mathbf{u} - \mathbf{f} + r\,\mathbf{g}$ for $d_p = 50\,\mu m$. Note that inertial particles have their common coreline (•) later down the flow.

Fig. 9. The STUART VORTEX at time $t = 0$. Particles are seeded repeatedly at the left border of the image. Essentially, this resembles a particle-based streakline construction. Streaklines proved useful for the observation of swirling behavior of particles [31].

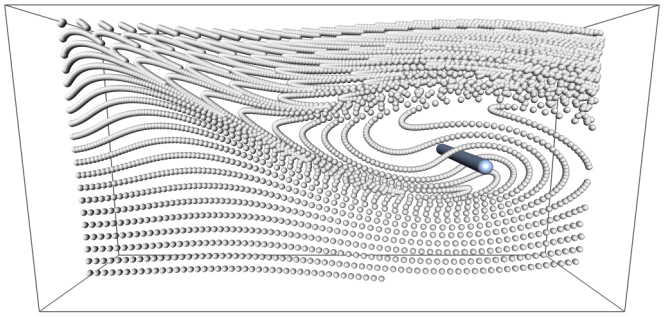

(a) Particles with $d_p = 0\,\mu m$ (massless) and their massless pathline core (•).

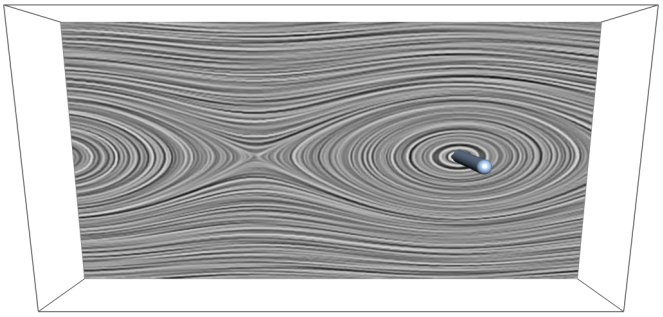

(b) LIC illustration of the vector field $\mathbf{u} - \mathbf{f} + r\,\mathbf{g}$ for $d_p = 0\,\mu m$ (massless).

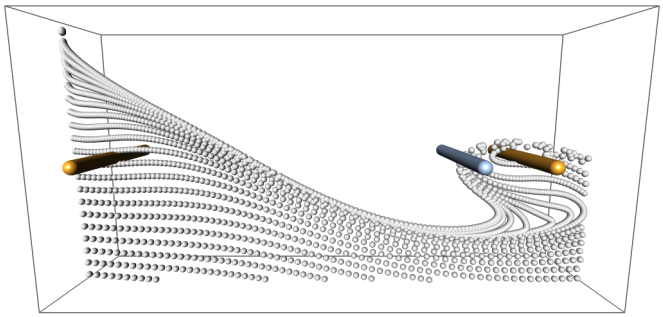

(c) For inertial particles with $d_p = 50\,\mu m$ a second inertial coreline appears.

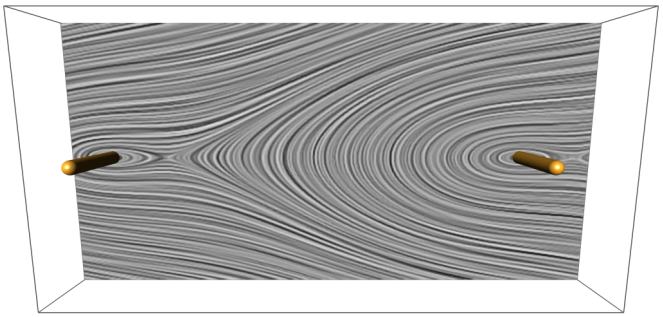

(d) The second vortex is apparent in the LIC of the vector field $\mathbf{u} - \mathbf{f} + r\,\mathbf{g}$ for $d_p = 50\,\mu m$.

Fig. 10. The STUART VORTEX at time $t = 1$. All particles and their vortices move to the right over time. As the field is periodic, other vortices will enter from the left.

Copyright (c) 2014 IEEE. Personal use is permitted. For any other purposes, permission must be obtained from the IEEE by emailing pubs-permissions@ieee.org.

This is the author's version of an article that has been published in this journal. Changes were made to this version by the publisher prior to publication.
The final version of record is available at http://dx.doi.org/10.1109/TVCG.2014.2346415

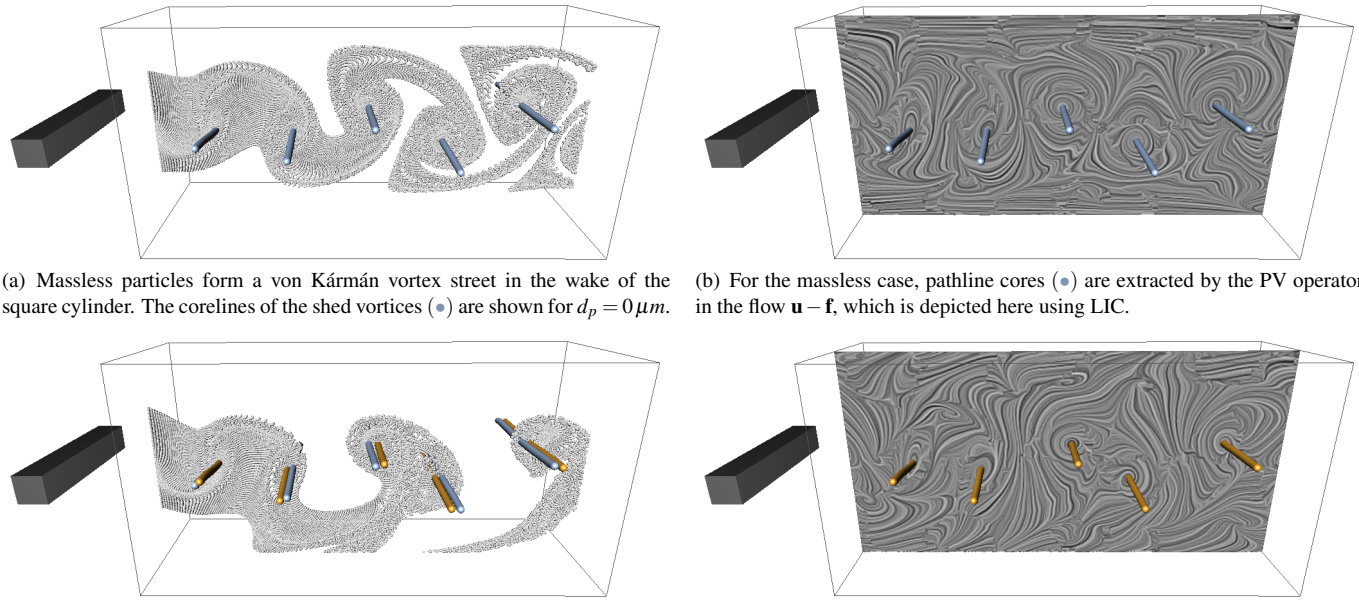

(a) Massless particles form a von Kármán vortex street in the wake of the square cylinder. The corelines of the shed vortices (•) are shown for $d_p = 0\,\mu m$.

(b) For the massless case, pathline cores (•) are extracted by the PV operator in the flow $\mathbf{u}-\mathbf{f}$, which is depicted here using LIC.

(c) Due to gravity, inertial particles, here with $d_p = 50\,\mu m$, do not form a perfectly symmetric vortex street. Their pathline cores (•) are shown to differ slightly from the massless case (•).

(d) The cores of swirling inertial particles (•) are extracted by applying the PV operator to the flow $\mathbf{u}-\mathbf{f}+r\,\mathbf{g}$. This flow is shown by LIC.

Fig. 11. Extraction results in the SQUARE CYLINDER sequence at time $t = 88$. Particles are released on the left hand side of the domain.

blue coreline, shown in Fig. 9(a). This massless pathline core can be found by standard PV extraction methods on the field $\mathbf{u}-\mathbf{f}$, as demonstrated in Section 4.3. Fig. 9(b) shows a LIC of this field, revealing the core centers. The inertial particles are subject to gravity and inertia, which affects the trajectories considerably. In fact, a number of particles exit the domain because of them. First the particles, released at the left hand side of the image, fall down, and are then uplifted by the vortex above. The inertial particles exhibit a swirling behavior later down the flow, which can be seen by the particles in Fig. 9(c). The common center of rotation is apparent by the translated coreline, found in the derived flow field in Fig. 9(d). It is noticeable that the massless and the inertial coreline differ.

The difference is clearer in the next time step, shown in Fig. 10. In the moving STUART VORTEX flow, the vortices advance in x-direction. Since the flow is periodic, a new coreline enters from the left in Fig. 10(c). While the rotation of the newly entering vortex is not very prominent in the particle visualization (as it is located shortly behind the seeding line), the LIC visualization of the derived vector field $\mathbf{u}-\mathbf{f}+r\,\mathbf{g}$ in Fig. 10(d) is clearly showing the streamline core that our method extracts.

5.7 Square Cylinder (3D unsteady)

The SQUARE CYLINDER sequence shows the development of a von Kármán vortex street, i.e., a periodic shedding of vortices in the unsteady flow around an obstacle. In this case, the obstacle is a confined square cylinder that is positioned symmetrically between two parallel walls. The incompressible fluid flow solution was computed by Camarri et al. [5] by the use of a direct Navier-Stokes solver. A uniformly resampled version of the flow was provided by Tino Weinkauf.

Fig. 11(a) shows the von Kármán vortex street for massless particles. The pathline cores are extracted by the parallel vectors operator on the field $\mathbf{u}-\mathbf{f}$, which is shown via LIC in Fig. 11(b). As shown in Fig. 11(c), the inertial particles with $d_p = 50\,\mu m$ are pulled down by the gravity with $\mathbf{g} = (0, -9.8065, 0)^{\mathrm{T}}$ and as a consequence, some of them exit the domain at the bottom. The remaining particles are lifted up and are trapped by the shed vortices. Their centers of rotation are shown in Fig. 11(d), together with the massless cores for reference. It can be seen that the inertial corelines differ from the massless case. The inertial cores were extracted on the field $\mathbf{u}-\mathbf{f}+r\,\mathbf{g}$, which is visualized in Fig. 11(d).

6 IMPLEMENTATION AND EVALUATION

6.1 Coreline Extraction and Filtering

In Section 4, we have shown that the extraction of inertial pathline cores can be reduced to a parallel vectors operation. Therefore, any of the existing PV extraction methods can be used, see Peikert and Roth [18] for a comprehensive overview. Because of this, our method can be easily integrated into standard visualization libraries. In fact, we implemented the extraction process in the visualization toolkit Amira [25] by using existing standard modules. Only the integration of inertial particle trajectories was precomputed in a separate tool, for which we used a fourth-order Runge-Kutta integrator.

Peikert and Roth [18] have shown an analytic parallel vectors solution for triangles, which is implemented in Amira and works as follows. First, a uniform grid is placed in the domain. Its resolution is shown for our data sets in Table 2. Following the recommendation of Weinkauf and Theisel [30], we used the resolution of the data sets. For every grid vertex that has complex eigenvalues, i.e., exhibits swirling behavior, the two vector fields are computed according to Table 1. Then, each face of the grid cells is subdivided into two triangles at which the locations of parallelity are computed analytically. In a next step, the line segments of adjacent cells are merged if the tangent is aligned and the end points are identical.

Afterwards, the resulting line set is further filtered to only contain line segments that are tangential to the parallel vectors, which is standard procedure for Sujudi-Haimes. Then, to fill in gaps, lines search near their endpoints for nearby segments to join with. Eventually, lines are filtered by length by a threshold given in Table 2. An unfiltered result is shown in Fig. 12.

Data Set (Section)	Grid Resolution	Filter Length
MOVING CENTER (5.1)	64×64×64	—
BEADS FLOW (5.2)	64×64×128	—
HELI DESCENT (5.3)	192×262×309	13.5
DELTA WING (5.4)	250×125×100	4.3
HURRICANE (5.5)	64×64×64	8.0
STUART VORTEX (5.6)	128×64×64	—
SQUARE CYLINDER (5.7)	192×64×48	1.0

Table 2. Grid resolutions used for the parallel vector operator and the used filter lengths, given in the unit of the data set scale.

Copyright (c) 2014 IEEE. Personal use is permitted. For any other purposes, permission must be obtained from the IEEE by emailing pubs-permissions@ieee.org.

This is the author's version of an article that has been published in this journal. Changes were made to this version by the publisher prior to publication.
The final version of record is available at http://dx.doi.org/10.1109/TVCG.2014.2346415

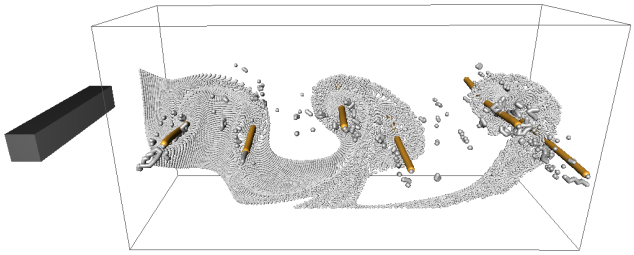

Fig. 12. The coreline extraction by parallel vectors creates a number of false positives (•), which are usually filtered. In this image, the filtering by approximate tangent alignment with the parallel vectors is disabled. The corelines are shown (•) in the SQUARE CYLINDER for $t = 94.2$.

Data Set (Section)	Field f	Coreline	Filtering
MOVING CENTER (5.1)	—	15.21 s	—
BEADS FLOW (5.2)	—	29.68 s	—
HELI DESCENT (5.3)	—	57.18 s	2.27 ms
DELTA WING (5.4)	—	6.43 s	0.48 ms
HURRICANE (5.5)	—	1.49 s	2.49 ms
STUART VORTEX (5.6)	1.87 s	7.79 s	—
SQUARE CYLINDER (5.7)	1.08 s	13.67 s	4.30 ms

Table 3. Timings for the individual computation steps: Computation of the feature flow field $\mathbf{f}$ (only for unsteady data), the extraction of the corelines in Amira, and the runtime of the additionally applied filtering, if it was necessary.

6.2 Performance

Our test system is equipped with an Intel Core i7-2600K CPU with 3.4 GHz and 24 GB RAM. Table 3 lists the timings for the three steps in the extraction process. Note that these steps are the same as for the massless Sujudi-Haimes [26] using parallel vectors [18] and its unsteady variant [30]. For unsteady data, first the feature flow field $\mathbf{f}$ is computed, which took for the grid resolutions that we used less than two seconds. Then, the pathline cores are extracted in our derived vector field, resulting in the inertial pathline cores. For this, the standard parallel vectors module of Amira is used. In summary, this took less than a minute on all our test data sets, most of them in a span of just a few seconds. The runtime depends not only on the grid resolution, but also on the presence of swirling. The DELTA WING for instance, has a high resolution, but only few voxels exhibit swirling behavior, i.e., have complex-conjugate eigenvalues in the Jacobian, thus large portions of the domain can safely be skipped. In the MOVING CENTER and BEADS FLOW, on the other hand, every voxel has swirling behavior. For these two data sets, the runtime linearly scales with the resolution. The extraction can be significantly accelerated, if parallel vectors are computed in a region of interest, which can be found by manual inspection of the parallel vector fields. In the SQUARE CYLINDER, for instance, this reduced the extraction time from $13.67\,s$ to $1.58\,s$. Finally, it is common to filter the extracted line geometry to only keep lines that are approximately tangential to the parallel vectors. This step is in the order of milliseconds. If the filtering was not required for a particular data set, we left the entry in the table blank. In general, the overhead for the consideration of inertial properties is compared to the massless case *close to zero*. In its essence, only the constant vector field $r\,\mathbf{g}$ is added prior to the standard extraction, which takes about 0.002%–0.08% of the total extraction time.

Since all operations are local, the computation of the PV operator can be done iteratively per cell without memory overhead. In fact, the memory scales linearly with the size of the output coreline set.

For the time-periodic BEADS FLOW in Section 5.2, the integration-based method took about 1.1 seconds. Since all particles are attracted by the same coreline, we only had to integrate one group of 5 particles. Once they converged, we continued the integration by one time period to record the complete coreline.

6.3 Limitations

Even for the massless case, the existing vortex coreline extractors are not able to handle all scenarios. The local method of Sujudi and Haimes [26] only finds corelines moving along straight lines (or not moving at all). Weinkauf and Theisel [31] have shown that an application of the method of Sujudi and Haimes to pathlines [30], does not reveal the apparent attractor in the BEADS FLOW. The integration-based methods [33, 31], on the other hand, only detect attracting corelines. A simple data set in which none of the methods will work is a center moving along an ellipse. As our techniques are extensions of existing methods from the massless to the inertial case, they do not fill these gaps.

When considering time sequences, the coreline is extracted for each frame individually. A problem of standard local PV extractors is that they do not explicitly enforce frame coherence, which is apparent in the slightly oscillating corelines of the SQUARE CYLINDER sequence in the accompanying video.

Also Sujudi-Haimes cannot extract a coreline if a real eigenvalue is zero, i.e., $\det \mathbf{J} = 0$. This happens, for instance, in a center without movement in the non-swirling direction: $\mathbf{u}(x,y,z) = (-z,0,x)^{\mathrm{T}}$. This case can be detected and then handled with 2D techniques, since in the swirling plane, spanned by the eigenvectors to the complex-conjugate eigenvalues, the velocity magnitude will vanish to zero at the coreline.

The advantage of the Sujudi-Haimes method in terms of computation effort is that it is a local method. As a consequence, it detects corelines without regarding if particles could actually appear in a certain region of the flow. This, in turn, would actually require an integration of a large number of particles from the inlet zones to see if any of them is reaching the region in question. This has an implication for inertial vortex cores. Particles of a certain size might never reach higher altitudes due to gravity. Though, since our method is based on the local Sujudi-Haimes, vortex cores might be extracted that are never visited by particles of a certain size. This means, an additional (integration-based) filtering is in order. However, this filtering process is completely orthogonal to the coreline extraction and the performance advantages of being local are considerable.

7 CONCLUSION

In this paper, we extended an established local vortex coreline extractor for massless particles to the inertial case. The problem, actually in 6D or 7D (space, velocity and optional time), reduces to a 3D or 4D parallel vectors operation, which can be solved efficiently using standard implementations. The method is therefore easily added to existing flow analysis tools. In fact, except for the integration of inertial particles, we could implement all components in Amira [25] by using existing modules. Moreover, we demonstrated the use of an integration-based extractor that detects attracting corelines.

The particle model we used is designed for the prediction of small particles. If the velocity magnitude is high compared to the acting gravity, the resulting inertial corelines are quite similar for the masses considerable by the simplified inertial equations of motion. In fact, differences are observable in particular for low wind speeds. For this reason, we synthetically altered some of our test data to showcase the extraction of mass-dependent corelines. Further sources for differences are additional forces, such as buoyancy or drag, which are typically neglected for small particles. A derivation of a coreline extraction for larger inertial particles is an avenue for future research. Also the visual analysis of where and why differences occur is interesting; not only for the analysis of vortex cores, but also for mass-dependent integral curves. Considering the uncertainty of vortices of inertial particles in the spirit of [17] is also an interesting topic. A more quantitative evaluation, including inertial particles and fluids of different densities might help to better understand the underlying physical effects. So far, we extended the local Sujudi-Haimes and the integration-based particle density estimation. Another possibility to explore is to apply the streakline-based extraction method of Weinkauf and Theisel [31].

Copyright (c) 2014 IEEE. Personal use is permitted. For any other purposes, permission must be obtained from the IEEE by emailing pubs-permissions@ieee.org.

This is the author's version of an article that has been published in this journal. Changes were made to this version by the publisher prior to publication.
The final version of record is available at http://dx.doi.org/10.1109/TVCG.2014.2346415

References

[1] D. C. Banks and B. A. Singer. A predictor-corrector technique for visualizing unsteady flow. *IEEE Transactions on Visualization and Computer Graphics*, 1:151–163, 1995.

[2] D. Bauer and R. Peikert. Vortex tracking in scale-space. In *Proc. Symposium on Data Visualisation*, pages 233–240, 2002.

[3] J. Bec, L. Biferale, M. Cencini, A. S. Lanotte, and F. Toschi. Spatial and velocity statistics of inertial particles in turbulent flows. *Journal of Physics: Conference Series*, 333(1):012003, 2011.

[4] R. Benzi, L. Biferale, E. Calzavarini, D. Lohse, and F. Toschi. Velocity-gradient statistics along particle trajectories in turbulent flows: The refined similarity hypothesis in the lagrangian frame. *Phys. Rev. E*, 80:066318, Dec 2009.

[5] S. Camarri, M.-V. Salvetti, M. Buffoni, and A. Iollo. Simulation of the three-dimensional flow around a square cylinder between parallel walls at moderate Reynolds numbers. In *XVII Congresso di Meccanica Teorica ed Applicata*, 2005.

[6] C. M. Casciola, P. Gualtieri, F. Picano, G. Sardina, and G. Troiani. Dynamics of inertial particles in free jets. *Physica Scripta*, 2010(T142):014001, 2010.

[7] C. Crowe, M. Sommerfield, and Y. Tsuji. *Multiphase Flows with Droplets and Particles*. CRC Press, 1998.

[8] R. Fuchs, R. Peikert, H. Hauser, F. Sadlo, and P. Muigg. Parallel Vectors Criteria for Unsteady Flow Vortices. *IEEE Transactions on Visualization and Computer Graphics*, 14(3):615–626, 2008.

[9] T. Günther, A. Kuhn, B. Kutz, and H. Theisel. Mass-dependent integral curves in unsteady vector fields. *Computer Graphics Forum (Proc. EuroVis)*, 32(3):211–220, 2013.

[10] G. Haller. An objective definition of a vortex. *Journal of Fluid Mechanics*, 525:1–26, 2005.

[11] G. Haller and T. Sapsis. Where do inertial particles go in fluid flows? *Physica D Nonlinear Phenomena*, 237:573–583, 2008.

[12] J. C. R. Hunt. Vorticity and vortex dynamics in complex turbulent flows. *Transactions on Canadian Society for Mechanical Engineering (Proc. CANCAM)*, 11(1):21–35, 1987.

[13] J. Jeong and F. Hussain. On the identification of a vortex. *Journal of Fluid Mechanics*, 285:69–94, 1995.

[14] B. M. Kutz, T. Günther, A. Rumpf, and A. Kuhn. Numerical examination of a model rotor in brownout conditions. In *Proceedings of the American Helicopter Society, 70th Annual Forum*, number AHS2014-000343, May 2014.

[15] R. S. Laramee, H. Hauser, L. Zhao, and F. H. Post. Topology-based flow visualization, the state of the art. In *Topology-based Methods in Visualization*, Mathematics and Visualization, pages 1–19. Springer Berlin Heidelberg, 2007.

[16] M. R. Maxey and J. J. Riley. Equation of motion for a small rigid sphere in a nonuniform flow. *Physics of Fluids*, 26(4):883–889, 1983.

[17] M. Otto and H. Theisel. Vortex analysis in uncertain vector fields. *Computer Graphics Forum (Proc. EuroVis)*, 31(3):1035–1044, 2012.

[18] R. Peikert and M. Roth. The "parallel vectors" operator – a vector field visualization primitive. In *Proc. IEEE Visualization*, pages 263–270, 1999.

[19] F. H. Post, B. Vrolijk, H. Hauser, R. S. Laramee, and H. Doleisch. The state of the art in flow visualisation: Feature extraction and tracking. *Computer Graphics Forum*, 22(4):775–792, 2003.

[20] S. Roettger, M. Schulz, W. Bartelheimer, and T. Ertl. Automotive soiling simulation based on massive particle tracing. In *Data Visualization 2001*, Eurographics, pages 309–317. Springer Vienna, 2001.

[21] M. Roth and R. Peikert. A higher-order method for finding vortex core lines. In *Proc. IEEE Visualization*, pages 143–150, 1998.

[22] J. Sahner, T. Weinkauf, and H.-C. Hege. Galilean invariant extraction and iconic representation of vortex core lines. In *Proc. Eurographics / IEEE VGTC Symposium on Visualization (EuroVis)*, pages 151–160, 2005.

[23] J. Sahner, T. Weinkauf, N. Teuber, and H.-C. Hege. Vortex and strain skeletons in Eulerian and Lagrangian frames. *IEEE Transactions on Visualization and Computer Graphics*, 13(5):980–990, 2007.

[24] Y. Shao and A. Li. Numerical modelling of saltation in the atmospheric surface layer. *Boundary-Layer Meteorology*, 91:199–225, 1999.

[25] D. Stalling, M. Westerhoff, and H.-C. Hege. Amira: A highly interactive system for visual data analysis. In *The Visualization Handbook*, pages 749–767. Elsevier, 2005.

[26] D. Sujudi and R. Haimes. Identification of swirling flow in 3D vector fields. Technical report, Departement of Aeronautics and Astronautics, MIT, 1995. AIAA Paper 95-1715.

[27] M. Syal, B. Govindarajan, and J. G. Leishman. Mesoscale sediment tracking methodology to analyze brownout cloud developments. In *Proc. American Helicopter Society, 66th Annual Forum*, 2010.

[28] H. Theisel, J. Sahner, T. Weinkauf, H.-C. Hege, and H.-P. Seidel. Extraction of parallel vector surfaces in 3D time-dependent fields and application to vortex core line tracking. In *Proc. IEEE Visualization*, pages 631–638, 2005.

[29] H. Theisel and H.-P. Seidel. Feature flow fields. In *Proc. Symposium on Data Visualisation*, pages 141–148, 2003.

[30] T. Weinkauf, J. Sahner, H. Theisel, and H.-C. Hege. Cores of swirling particle motion in unsteady flows. *IEEE Transactions on Visualization and Computer Graphics (Proc. Visualization)*, 13(6):1759–1766, 2007.

[31] T. Weinkauf and H. Theisel. Streak lines as tangent curves of a derived vector field. *IEEE Transactions on Visualization and Computer Graphics (Proc. Vis)*, 16(6):1225–1234, 2010.

[32] T. Weinkauf, H. Theisel, H.-C. Hege, and H.-P. Seidel. Feature flow fields in out-of-core settings. In *Proc. Topo-In-Vis 2005*, pages 51–64, 2007.

[33] A. Wiebel, R. Chan, C. Wolf, A. Robitzki, A. Stevens, and G. Scheuermann. Topological flow structures in a mathematical model for rotation-mediated cell aggregation. In *Topological Methods in Data Analysis and Visualization*, Mathematics and Visualization, pages 193–204, 2009.

[34] Y. Yu, C. Tung, B. van der Wall, H.-J. Pausder, C. Burley, T. Brooks, P. Beaumier, Y. D. E. Mercker, and K. Pengel. The HART-II test: Rotor wakes and aeroacoustics with higher-harmonic pitch control (HHC) inputs – the joint German/French/Dutch/US project. *American Helicopter Society 58th Annual Forum*, 2002.

[35] T. Zhu, D.-L. Zhang, and F. Weng. Impact of the advanced microwave sounding unit data on hurricane prediction. *Monthly Weather Review*, 130:2416–2432, 2002.

[36] T. Zhu, D.-L. Zhang, and F. Weng. Numerical simulation of hurricane bonnie (1998). part i: Eyewall evolution and intensity changes. *Monthly Weather Review*, 132:225–241, 2004.

Copyright (c) 2014 IEEE. Personal use is permitted. For any other purposes, permission must be obtained from the IEEE by emailing pubs-permissions@ieee.org.